Icarus 255 (2015) 148–158

Contents lists available at ScienceDirect

Icarus

journal homepage: www.elsevier.com/locate/icarus

Transport of water in a transient impact-generated lunar atmosphere

P. Prem [a,*], N.A. Artemieva [b], D.B. Goldstein [a], P.L. Varghese [a], L.M. Trafton [c]

[a] Department of Aerospace Engineering & Engineering Mechanics, The University of Texas at Austin, 210 East 24th Street, Austin, TX 78712-1221, United States
[b] Planetary Science Institute, 1700 East Fort Lowell, Suite 106, Tucson, AZ 85719-2395, United States
[c] Department of Astronomy, The University of Texas at Austin, 2515 Speedway, Austin, TX 78712-1205, United States

ARTICLE INFO

Article history:
Received 29 May 2014
Revised 29 August 2014
Accepted 10 October 2014
Available online 18 October 2014

Keywords:
Atmospheres, dynamics
Comets
Ices
Impact processes
Moon

ABSTRACT

In recent decades, several missions have detected signs of water and other volatiles in cold, permanently shadowed craters near the lunar poles. Observations suggest that some of these volatiles could have been delivered by comet impacts and therefore, understanding the impact delivery mechanism becomes key to explaining the origin and distribution of lunar water. During impact, the constituent ices of a comet nucleus vaporize; a significant part of this vapor remains gravitationally bound to the Moon, transforming the tenuous, collisionless lunar exosphere into a collisionally thick, transient atmosphere. Here, we use numerical simulations to investigate the physical processes governing volatile transport in the transient atmosphere generated after a comet impact, with a focus on how these processes influence the accumulation of water in polar cold traps. It is observed that the transient atmosphere maintains a certain characteristic structure for at least several Earth days after impact, during which time volatile transport occurs primarily through low-altitude winds that sweep over the lunar day-side. Meanwhile, reconvergence of vapor antipodal to the point of impact results in preferential redistribution of water in the vicinity of the antipode. Due to the quantity of vapor that remains gravitationally bound, the atmosphere is sufficiently dense that lower layers are shielded from photodestruction, prolonging the lifetime of water molecules and allowing greater amounts of water to reach cold traps. Short-term ice deposition patterns are markedly non-uniform and the variations that arise in simulated volatile abundance between different cold traps could potentially explain variations that have been observed through remote sensing.

1. Introduction

Over the years, a number of missions have observed signs of water and other volatiles in permanently shadowed craters ('cold traps') near the lunar poles (Feldman et al., 2000; Spudis et al., 2010; Colaprete et al., 2010; Gladstone et al., 2012). Due to the almost perpendicular orientation of the Moon's spin axis relative to the ecliptic, parts of the interiors of these craters have not seen sunlight for billions of years (Arnold, 1979) and have temperatures so low that a variety of volatile compounds, notably water, can remain stable at the surface and shallow sub-surface over geological time scales (Watson et al., 1961; Paige et al., 2010).

Water can reach the lunar surface in several ways; it can be degassed from the lunar interior, generated in situ by solar wind bombardment of the regolith or delivered by impacts of volatile-bearing bodies ranging in size from micrometeoroids to comets (Arnold, 1979; Morgan and Shemansky, 1991). Numerical models (Butler, 1997; Crider and Vondrak, 2000, 2002) suggest that some of the water supplied by these sources can subsequently migrate to polar cold traps. Several groups, most recently Miller et al. (2014), Zuber et al. (2012) and Neish et al. (2011), have used remote sensing data to derive constraints on the abundance and distribution of cold-trapped volatiles, but significant uncertainties remain regarding the nature and amount of water present. In this context, understanding source and delivery mechanisms becomes key to interpreting observations and to understanding the lunar volatile inventory.

Comet impacts are a delivery mechanism of particular interest. The LCROSS mission led to the detection of not only H_2O, but also CH_4, NH_3 and other compounds commonly found in comets, at the Cabeus cold trap (Colaprete et al., 2010). More recently, Miller et al. (2014) revisited neutron spectroscopy data from the Lunar Prospector mission and identified isolated sub-surface hydrogen signatures at some cold traps – the absence of a corresponding surficial signature suggesting delivery of the detected hydrogen (possibly water) by some ancient, episodic source. Lastly, it has been observed that water ice, if present, appears to be heterogeneously

* Corresponding author.
E-mail address: parvathy.prem@utexas.edu (P. Prem).

http://dx.doi.org/10.1016/j.icarus.2014.10.017
0019-1035/

distributed between cold traps, with some regions of permanent shadow lacking signs of water (Mitrofanov et al., 2010; Gladstone et al., 2012). These differences could partly be due to local variations in topography and thermal history (Siegler et al., 2011; Schorghofer and Taylor, 2007), but it could also be the case that certain delivery mechanisms, such as comet impacts, distribute volatiles non-uniformly between cold traps, further contributing to the heterogeneity of the signatures observed. Other delivery mechanisms, such as the cold-trapping of solar wind-generated volatiles, rely on collisionless migration of molecules to the poles, which should lead to uniform filling of cold traps, since the average ballistic hop distance is larger than typical cold trap dimensions (Watson et al., 1961).

Modeling comets as a source of lunar water is a complex problem. During impact, a cometary nucleus is subject to extreme pressures and temperatures, more than sufficient to completely vaporize constituent ices (Pierazzo and Melosh, 2000). Much of this vapor escapes lunar gravity within seconds, but a significant part remains gravitationally bound and can linger for months (Stewart et al., 2011) in the form of a transient atmosphere. The primary challenge in modeling this atmosphere lies in the fact that the sheer quantity of volatiles delivered by a comet impact significantly changes the way in which volatile transport takes place. Usually, the Moon's surface-bound exosphere is so tenuous, with surface densities $O(10^{10})$ molecules/m^3, that molecules rarely encounter each other, and can be assumed to migrate across the lunar surface through collisionless, ballistic hops (Stern, 1999; Cook et al., 2013). However, after a large-scale impact, the atmosphere can become sufficiently dense that gas dynamic processes are governed by collisions between molecules – these interactions are then no longer negligible. Moreover, in a sufficiently dense atmosphere, water vapor may be partially shielded from photodestruction (Arnold, 1979), the primary loss process. Shielding and other physical processes that become important in an impact-generated atmosphere – such as photochemical reactions (Berezhnoi and Klumov, 2000) and radiative heat transfer – can play a key role in determining the abundance and distribution of cold-trapped species.

Several prior investigations have focused on transport of volatiles in the collisionless limit – a valid approximation when the source of volatiles does not alter the tenuous nature of the lunar exosphere. For instance, Butler (1997) and Crider and Vondrak (2000, 2002) have used Monte Carlo methods to model the transport of solar wind-generated hydrogen and water to polar cold traps, tracking the migration of molecules from a globally distributed surficial source, through collisionless hops, until capture or photodestruction. Considering volatile-rich impacts as another source, Berezhnoi and Klumov (1998) estimated the amount of water that could be delivered by a comet to polar cold traps, based on an analytical approximation of how much impact-generated vapor would remain gravitationally bound given comet size, density and impact velocity. More recently, Ong et al. (2010) addressed this question in greater detail, using hydrocode simulations to study the dependence of volatile retention on impact velocity by tracking the fraction of non-escaping projectile material for a series of vertical impacts at different velocities. Determining the gravitationally bound fraction of impact-generated vapor under various impact parameters is an important step toward understanding the cometary contribution to the lunar volatile inventory, but how and how much of the gravitationally bound vapor ultimately reaches a cold trap is determined by the loss rate and gas dynamics of volatile transport in a collisionally thick, temporally evolving atmosphere.

Most previous studies have not explicitly addressed the qualitatively different nature of volatile transport in an impact-generated atmosphere. Berezhnoi and Klumov (1998) estimated that almost all gravitationally bound vapor would condense into cold traps, while Ong et al. (2010) applied the result of Butler (1997) to project that 20% of the gravitationally bound vapor would migrate to cold traps. Both of these approaches assumed diffusive transport of water vapor and neglected any shielding of lower layers of the atmosphere from photodestruction. Stewart et al. (2011) developed the approach adopted in this work and used the SOVA hydrocode and the Direct Simulation Monte Carlo (DSMC) method to simulate an oblique comet impact and to track the deposition of impact-generated water vapor in cold traps over the course of months (i.e. several lunar days). The hybrid SOVA–DSMC method accounts for the collisional character of the transient atmosphere and, although some simplifications were introduced, Stewart et al.'s (2011) work represents the most detailed treatment of post-impact gas dynamics to date.

The primary objective of Stewart et al. (2011) was to determine how much water from the simulated comet impact was transported to polar cold traps. Here, we focus on understanding post-impact volatile transport processes in more depth – characterizing the structure of the transient atmosphere generated by a large-scale impact on an otherwise virtually airless body and analyzing the implications of such an atmosphere for the transport and deposition of water at lunar cold traps. The Stewart et al. (2011) code has been modified to account for additional physical processes of significance; specifically, radiative cooling of water vapor and shielding of lower layers of the atmosphere from dissociating ultraviolet radiation.

In the sections that follow, we describe the numerical method used and then discuss results obtained for the evolution of a transient, impact-generated lunar atmosphere over the course of several Earth days after impact, focusing on characteristic atmospheric structures, their influence on the transport and deposition of water, and relation to remote sensing observations.

2. Numerical method

Stewart et al. (2011) provide a detailed description of the numerical method used in this work. Here, we briefly review the method and then discuss modifications that have been made to the physical model in order to simulate post-impact gas dynamics more accurately. We retain the hybrid SOVA–DSMC approach of Stewart et al. (2011), reviewed below.

To start with, the SOVA hydrocode (Shuvalov, 1999) is used to simulate the immediate physics of a comet impact: the phase changes that occur in both target and projectile due to the passage of successive compression and rarefaction waves, and the resultant hydrodynamic flow of molten and vaporized target and projectile material. The simulations discussed here consider a comet that impacts the Moon at 30 km/s and at an angle of 60° (measured from the horizontal). The lunar surface is assigned the material properties of dunite, and the comet is modeled as a sphere of pure water ice, 2 km in diameter.

Hydrocodes use a continuum description of material behavior, which is accurate when modeling the initially dense plume of impact-generated vapor. However, as the plume expands into a near vacuum background, it undergoes rapid rarefaction and transitions from a dense, continuum regime close to the point of impact to collisionless at the outermost fringes of the expanding cloud. Due to the ultimately non-continuum behavior of the impact-generated vapor, the SOVA simulations are limited to a hemispherical domain extending out to 20 km from the point of impact. Subsequent modeling of impact-generated water vapor is carried out using the Direct Simulation Monte Carlo (DSMC) method (Bird, 1994). Although the impact-generated plume consists of both water vapor and vaporized or molten rock, in this

study we focus on the water vapor component (as in Stewart et al., 2011) and neglect any water–rock interactions outside the SOVA domain. Fig. 1 is a schematic depiction of the interfacing between the two codes (described and validated in Stewart et al., 2009) and the problem set-up. Both DSMC and SOVA simulations are unsteady and three-dimensional.

DSMC is a statistical method that models gas behavior by moving and colliding a large number of representative molecules within a gridded domain. This approach is particularly useful in regimes where flow is still collisional, but the continuum description begins to break down – such as during expansions into vacuum, when a gas may become so rarefied that the mean distance between molecular collisions is larger than characteristic length scales of the problem. Under these circumstances, gas behavior must be described using the Boltzmann equation, analytical solution of which is usually prohibitively complex. Instead, numerical methods such as DSMC have commonly been used for similar problems in planetary science with considerable success (for instance, Combi, 1996; Walker et al., 2010; Cassidy and Johnson, 2010). The accuracy of the DSMC method increases with the number of representative molecules simulated – in the limit of a large number of representative molecules, basic DSMC collision models have been shown to accurately represent the Boltzmann equation collision integral (Nanbu, 1986).

The DSMC simulations presented here were carried out using $O(10^8)$ particles and $O(10^7)$ cells. As described by Stewart et al. (2011), the simulations are performed in a series of staged computational domains of increasing size to account for the rapid expansion of impact-generated vapor to completely surround the Moon. In the quasi-cylindrical innermost domain (32 km × 32 km × 360°), cells are 100 m × 100 m × 1° in size and the time-step is 0.5×10^{-3} s. Later, global simulations of volatile transport are carried out in a domain bounded by two spherical surfaces: the lower boundary represents the lunar surface, and the upper boundary is at an altitude of 50,000 km. Cells are 1° × 2° in size in the azimuthal and polar dimensions respectively, while cell size in the radial dimension increases exponentially from 1 km at the lunar surface to 100 km above an altitude of ~60 km, with a collisionless "buffer" cell ~10,000 km in size to track molecules moving beyond ~40,000 km from the surface. In this domain, the time-step is varied from 1 s to 10 s as the atmosphere becomes less collisional with time. Due to the wide range of spatial and temporal scales of the problem, our simulations are under-resolved (i.e. cell size is larger than the mean free path and time-step is larger than the mean collision time) over large parts of the atmosphere, particularly in dense regions close to the lunar surface, where the mean free path is O(0.1 m) even hours after impact. Large cells introduce an unphysical numerical viscosity into the problem, which tends to smear gradients in macroscopic properties due to collisions between molecules within each cell that are separated by distances considerably larger than the mean free path. In order to reduce the inaccuracy introduced by large cells, we use a "free cell" routine (Roveda et al., 2000; Stewart et al., 2011) that preferentially collides nearby molecules in each cell. Although the simulations still remain under-resolved in some regions, we appear to be able to capture gradients in macroscopic properties, such as density and temperature, with reasonable accuracy.

At each time-step, the No Time Counter (NTC) scheme developed by Bird (1994) is used to determine a number of pairs of molecules to be selected within each computational cell. Collisions between molecules are then computed using the Variable Hard Sphere (VHS) model, according to which the molecules in each selected pair may or may not collide, depending on their relative velocity. Translational–rotational energy exchange between molecules during collisions is modeled using the standard Larsen-Borgnakke model, while translational–vibrational energy exchange is modeled using the discrete Larsen-Borgnakke model. We also use the collision limiting scheme developed by Stewart et al. (2009), which reduces the computational cost of simulations by accounting for the fact that in regions at local thermal equilibrium, only a limited number of collisions is required to bring the gas to equilibrium; subsequent collisions simply redistribute energy between molecules without affecting macroscopic properties.

As described by Stewart et al. (2011), our DSMC code is parallelized for computational speed and includes variable gravity, a photodestruction probability for molecules in sunlight, a simple, diurnally varying surface temperature map and temperature-dependent residence times for water molecules that land on the lunar surface. We compute the surface residence time, t_{res}, for an H_2O molecule on an H_2O matrix, given by the Langmuir (1916) and Frenkel (1924) model as:

$$t_{res} = \nu_0^{-1} \exp(\Delta H / k_B T_{surf}), \quad (1)$$

where $\Delta H = 6.65 \times 10^{-20}$ J is the binding energy for an H_2O molecule at the surface of an H_2O matrix, k_B is the Boltzmann constant, $\nu_0 = 2.0 \times 10^{12}$ s^{-1} is the lattice vibrational frequency of an H_2O molecule within an H_2O matrix, and T_{surf} is the surface temperature (Sandford and Allamandola, 1993). The main reason that we use H_2O on H_2O residence times is that it is probable that the lunar surface becomes rapidly saturated with several monolayers of water after a comet impact. Furthermore, based on data from the M^3 instrument on Chandrayaan-1, Li and Milliken (2013) estimate surface hydration levels of ~100–500 ppm (thought to be partly indigenous, and partly due to solar wind implantation) even at mid-to-low latitudes, suggesting that parts of the lunar surface

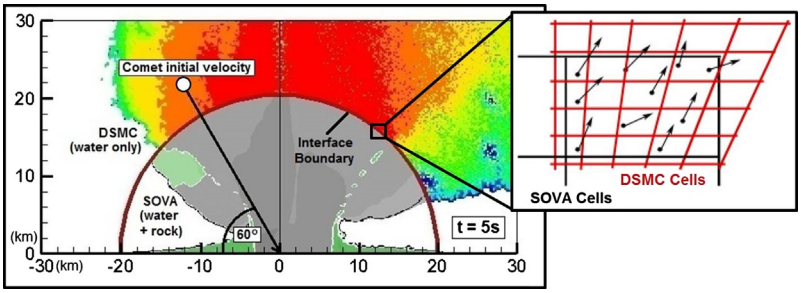

Fig. 1. Schematic depiction of the hybrid SOVA–DSMC approach, showing a two-dimensional cross-section (in the plane of impact) of SOVA and DSMC density contours, 5 s after a 60°, 30 km/s impact. The initial velocity vector is marked, and the comet is drawn approximately to scale. Also indicated is the boundary of the hemispherical interface separating the SOVA and DSMC computational domains. The inset diagram depicts the overlap between SOVA and DSMC cells at the interface, where DSMC molecules are initialized using continuum SOVA data for water vapor (gray). See Stewart et al. (2009, 2011) for details. (For interpretation of the references to color in this figure legend, the reader is referred to the web version of this article.)

may be coated by an adsorbed monolayer of water even before a comet impact.

Given the impact velocity and comet composition we have modeled, virtually all of the projectile is vaporized. Since atmospheric condensation into droplets or ice crystals is not currently modeled, molecules remain in the vapor phase until escape, destruction or capture. Seven regions of permanent shadow (six at the South Pole and one at the North Pole) are specified, and any molecule that lands in these regions is assumed to be permanently cold-trapped. Currently, photodestruction and cold trapping are the only atmospheric loss processes modeled. Although impact-generated vapor is initially heated to temperatures sufficiently high that some amount may dissociate, it is probable that dissociation products recombine as the (still dense) vapor cools rapidly during expansion into vacuum. By the time water vapor reaches the interface between the SOVA and DSMC codes, temperatures are well below 1000 K and pressures are O(1 atm). Under these conditions, water molecules should largely be in an undissociated state.

The primary changes made to the DSMC physical model for the purposes of this work have been the inclusion of shielding from photodestruction and radiative cooling of water molecules. Water is currently the only species modeled in the DSMC code and any shielding or radiative effects of vaporized target material or lofted, granular ejecta are not considered.

2.1. Shielding from photodestruction

Stewart et al. (2011) treated the transient atmosphere as optically thin in the ultraviolet i.e. all molecules other than those in the Moon's shadow were assumed to be exposed to unattenuated sunlight. In reality, the atmosphere can be sufficiently thick that the upper, sunward layers absorb a significant part of the solar ultraviolet, reducing the intensity of dissociating radiation that penetrates through to lower layers. More strongly illuminated parts of the vapor cloud are thus preferentially depleted, and the overall rate of photodestruction is reduced. Since photodestruction is the primary loss process for gravitationally bound water, reduced loss rates could significantly increase the amount of water that is captured, by providing more time for molecules to migrate to cold traps.

The photodestruction rate coefficient, r_{photo} (s^{-1}) within a given computational cell is computed as:

$$r_{photo} = (1.2\times10^{-5})[0.4\exp(-nL\sigma_{121.6\mathrm{nm}}) + 0.6\exp(-nL\sigma_{145-186\mathrm{nm}})] \quad (2)$$

Here, nL is the density of the atmospheric column (molecules/m^2) that sunlight passes through before it reaches the cell. Dissociation by the 121.6 nm Lyman-α line and by continuum absorption (Watanabe and Zelikoff, 1953) in the 145–186 nm range are considered separately. Based on the work of Crovisier (1989), Eq. (2) approximates 40% of photodestruction of H_2O in unattenuated sunlight to be due to Lyman-α and 60% to be due to ultraviolet radiation in the 145–186 nm range. For the quiet Sun, the total unattenuated photodestruction rate of H_2O at 1 AU is $1.2\times10^{-5}\ s^{-1}$ (Huebner et al., 1992). The parameter $\sigma_{121.6\mathrm{nm}}$ is the Lyman-α absorption cross-section (m^2) of an H_2O molecule and $\sigma_{145-186\mathrm{nm}}$ is a band-averaged absorption cross-section over the 145–186 nm range. Using data acquired by Watanabe and Zelikoff (1953), $\sigma_{121.6\mathrm{nm}}$ is found to be $1.571\times10^{-21}\ m^2$ and $\sigma_{145-186\mathrm{nm}}$ is found to be $2.384\times10^{-22}\ m^2$, approximating the Sun as a black body at 5780 K. Calculations of column density, nL, are performed periodically to account for changes in atmospheric structure and the position of the Sun. Since the computational domain is divided between processors for parallelization of the code, the DSMC grid sections contained in each processor are mapped to a single, non-uniform but still relatively coarse Cartesian grid, on which column density calculations are carried out; this approach strikes an acceptable balance between accuracy and computational speed.

Photodestruction is implemented in DSMC by deriving the probability, p_{photo}, that a molecule may dissociate during a timestep Δt:

$$p_{photo} = 1 - \exp(-r_{photo}\Delta t), \quad (3)$$

where r_{photo} is obtained from Eq. (2). Currently, photodissociation/ionization products are neglected; therefore, when a water molecule dissociates, it is simply removed from the simulation. It should, however, be noted that photochemical reactions involving H_2O and daughter species (such as H, OH, H_2 and O) could play a significant role in determining the composition and fate of the transient atmosphere. This problem could be addressed in subsequent work by creating daughter molecules with ejection velocities sampled from an appropriate distribution during each dissociation event and accounting for the probability that species may react during collisions.

2.2. Radiative cooling

Stewart et al. (2011) observed that water vapor generated by an impact could remain aloft for several days before falling back to the lunar surface. Over such time scales, a large part of the transient atmosphere is likely to become transparent to infrared radiation, allowing molecules to lose and gain internal energy through spontaneous emission and absorption of solar infrared radiation, respectively. Radiative cooling is a purely molecular phenomenon that can readily be modeled using DSMC. We model the loss of rotational energy (through spontaneous emission) by adopting an approach similar to that of Combi (1996), using the H_2O cooling rate expression specified by Gombosi et al. (1986) based on work by Crovisier (1984). Accordingly, in transparent surroundings, molecules lose rotational energy at a rate, Q_{rad} (W/molecule) given by:

$$Q_{rad} = \begin{cases} (4.4\times10^{-29})T_{rot}^{3.35} & \text{for } T_{rot} < 52\ \mathrm{K} \\ (2.0\times10^{-27})T_{rot}^{2.47} & \text{for } T_{rot} \geqslant 52\ \mathrm{K} \end{cases} \quad (4)$$

Here, T_{rot} is the rotational temperature of the molecule, related to its rotational energy E_{rot} through the Boltzmann constant k_B by the expression:

$$E_{rot} = (3/2)k_B T_{rot} \quad (5)$$

It should be noted that radiative cooling only affects translational temperature when molecules exchange rotational and translational energy through collisions. When solar heating is taken into account, Q_{rad} as calculated in Eq. (4) is modified by the subtraction of 6.835×10^{-25} W/molecule, a band-averaged value over the 10–500 μm range obtained using molecular absorption coefficients from the HITRAN database and approximating the Sun as a black body at 5780 K.

The implementation described above makes several simplifying assumptions. Firstly, we assume that the transient atmosphere is completely transparent to infrared radiation in the band of interest. This is not strictly the case, as spontaneously emitted radiation may be reabsorbed within the atmosphere rather than escaping completely, and solar infrared radiation may be attenuated before it reaches the inner regions of the vapor cloud. Another aspect of the radiative heat transfer problem that is currently not modeled is the heating of vapor by infrared radiation from the lunar surface, which has temperatures in the 120–400 K range and thus radiates strongly in the infrared. This radiation too is attenuated by distance and the presence of an absorbing atmosphere, but may be

the dominant source of radiant infrared energy for molecules near the surface.

Furthermore, in addition to rotational energy, water molecules may also lose vibrational energy through spontaneous emission. The probability (p_{emit}) that a molecule with its ith vibrational mode (i = 1, 2, 3 for H_2O) excited to level n, transitions from level n to level $(n-1)$ in a time interval Δt is given by:

$$p_{emit} = 1 - \exp(-r_{emit}\Delta t) \tag{6}$$

Here, we adopt the approach of Zhang et al. (2003) and consider only spontaneous emission (i.e. stimulated emission due to solar radiation is not considered), in which case the parameter r_{emit} is given by $nA_{i,1\to0}$, where $A_{i,1\to0}$ is the Einstein A coefficient corresponding to the $1 \to 0$ transition of the ith mode, and we assume (after Penner, 1959) that $A_{i,n\to n-1} = nA_{i,1\to0}$. Due to rapid cooling of impact-generated vapor during expansion and the relatively high characteristic vibrational temperatures of water ($\Theta_{v,1}$ = 5261 K, $\Theta_{v,2}$ = 2438 K and $\Theta_{v,3}$ = 5404 K), molecules largely remain in the vibrational ground state, where the probability of excitation through absorption is at its lowest; should a molecule be excited to a higher state, the probability that it will spontaneously de-excite is several orders of magnitude greater than the probability that it will be excited further. Thus, since vibrational modes are of less importance, the DSMC code does not presently account for coupling between solar mid-infrared radiation and vibrational energy of the H_2O molecule.

3. Results and discussion

3.1. Initial expansion and fallback

Fig. 2 shows cross-sectional views (in the plane of impact) of the transient atmosphere at seconds, minutes and hours after impact. Due to the oblique nature of the impact, the initial vapor plume (Fig. 2(a)) is asymmetric, with most of the vaporized projectile material expanding downrange of the direction of impact. Much of the vapor that is expanding away from the point of impact at this stage travels at speeds far higher than lunar escape velocity (~2380 m/s at the surface) and is not gravitationally bound. However, it is apparent from the nested shells of constant velocity in Fig. 2(a) that vapor emerging at later times travels at progressively lower speeds. Within the hour, slower, gravitationally bound vapor begins to fall back to the lunar surface (Fig. 2(b)) and the transient atmosphere acquires a characteristic structure (Fig. 2(c)).

3.2. Structure of the transient atmosphere

The transient atmosphere maintains the characteristic structure depicted in Fig. 2(c) for around 48 h, until all gravitationally bound vapor has begun to fall back or has crossed the Moon's Hill sphere (~60,000 km in radius). It should be noted that our simulations track water vapor only out to 50,000 km from the lunar surface, thereby neglecting the small fraction of vapor that begins to fall back only beyond this distance, or goes into orbit around the Earth.

Several hours after impact (Fig. 2(c)), high-altitude streamlines form a near-spherical, off-centered envelope; vapor within this envelope falls back to the Moon, while vapor outside continues to expand away. Since vapor that is faster to begin with travels further and takes longer before it starts to fall back, the fallback envelope becomes progressively larger with time. The growth of the fallback envelope can be approximated analytically by considering the evolution of nested shells of constant velocity (as seen in Fig. 2(a)) under variable gravity, treating each shell as though it is made up of non-interacting tracer particles, governed by the following equations of motion:

$$\begin{aligned} dv_r/dt &= -GM/r^2 \quad & dr/dt &= v_r \\ dv_\theta/dt &= 0 & r\,d\theta/dt &= v_\theta \end{aligned} \tag{7}$$

where r is radial distance and θ is polar angle; v_r and v_θ are velocities in the r and θ directions respectively, t is time, G is the gravitational constant and M is the mass of the Moon. When $v_r = 0$, a tracer particle begins to fall back, marking the boundary of the fallback envelope at that time.

This analytical treatment is possible because, although the vapor is collisional, the high velocities and low temperatures acquired during expansion and cooling mean that at high altitudes, molecular trajectories are close to ballistic. Therefore, although non-interacting tracer particles cannot capture gas dynamic interactions such as those which occur antipodal to the point of impact, Eq. (7) can be used to estimate the size of the fallback envelope at a given time with reasonable accuracy. Fig. 3 demonstrates the close agreement between simulated and analytically derived values of a representative dimension, $R_{fallback}$ (the radial distance from the center of the Moon to the fallback envelope as measured through the point of impact), which can be calculated by setting $v_\theta = 0$ for a tracer particle moving radially outward (relative to the center of the Moon) and using Eq. (7) to compute $R_{fallback}$ (the radial distance at which $v_r = 0$) as a function of time.

The structure of the atmosphere directly influences the redistribution of cometary water about the lunar surface. In addition to the fallback envelope, another phenomenon visible in Fig. 2(c) is the reconvergence of streamlines antipodal to the North Pole point of impact as the expanding vapor cloud closes around the Moon. Since the expanding vapor is traveling at supersonic speeds, reconvergence leads to the formation of an approximately cylindrical atmospheric shock structure that channels vapor down toward the lunar surface. Antipodal effects have previously been explored in other contexts (such as Hood and Artemieva, 2008), but here, our finding that after any sufficiently large-scale release of volatiles, an atmospheric shock leads to preferential redistribution of water in the vicinity of the antipode is particularly significant. In the present simulations, the impact location is such that the antipodal shock directly intersects the cold night-side; if instead, the antipode happened to be located on the day-side, the antipodal shock would still drive a concentrated jet of water vapor down toward the surface, but interaction of this jet with day-side winds could lead to more complex deposition patterns. Despite the asymmetry of the initial vapor plume, it is seen that antipodal reconvergence occurs in an almost symmetric manner, since the slower, late-emerging vapor that remains gravitationally bound and reconverges during fallback tends to be less strongly downrange focused than the high-velocity early component. Moreover, any effect of centrifugal and Coriolis forces appears minimal on the slowly rotating Moon.

It should be noted that the antipodal shock results from the collisional nature of the atmosphere. If the atmosphere were collisionless, molecules would simply stream past each other as the expanding flow reconverged; the abrupt turning and compression of water vapor caused by the shock would be absent, and there would be no preferential redistribution around the antipode.

The collisional nature of the transient atmosphere also gives rise to relatively dense, low-altitude winds over the day-side hemisphere. When water molecules come into contact with the lunar surface, they are modeled to have a temperature-dependent residence time before being diffusely scattered. Molecules falling back to the cold lunar night-side, where the residence time is ~37 h, are largely immobilized until sunrise. In contrast, molecules falling back to the warm lunar day-side have much shorter residence times (O(0.1 μs) at the sub-solar point) and remain aloft, giving rise to a relatively dense, low-altitude, day-side atmosphere

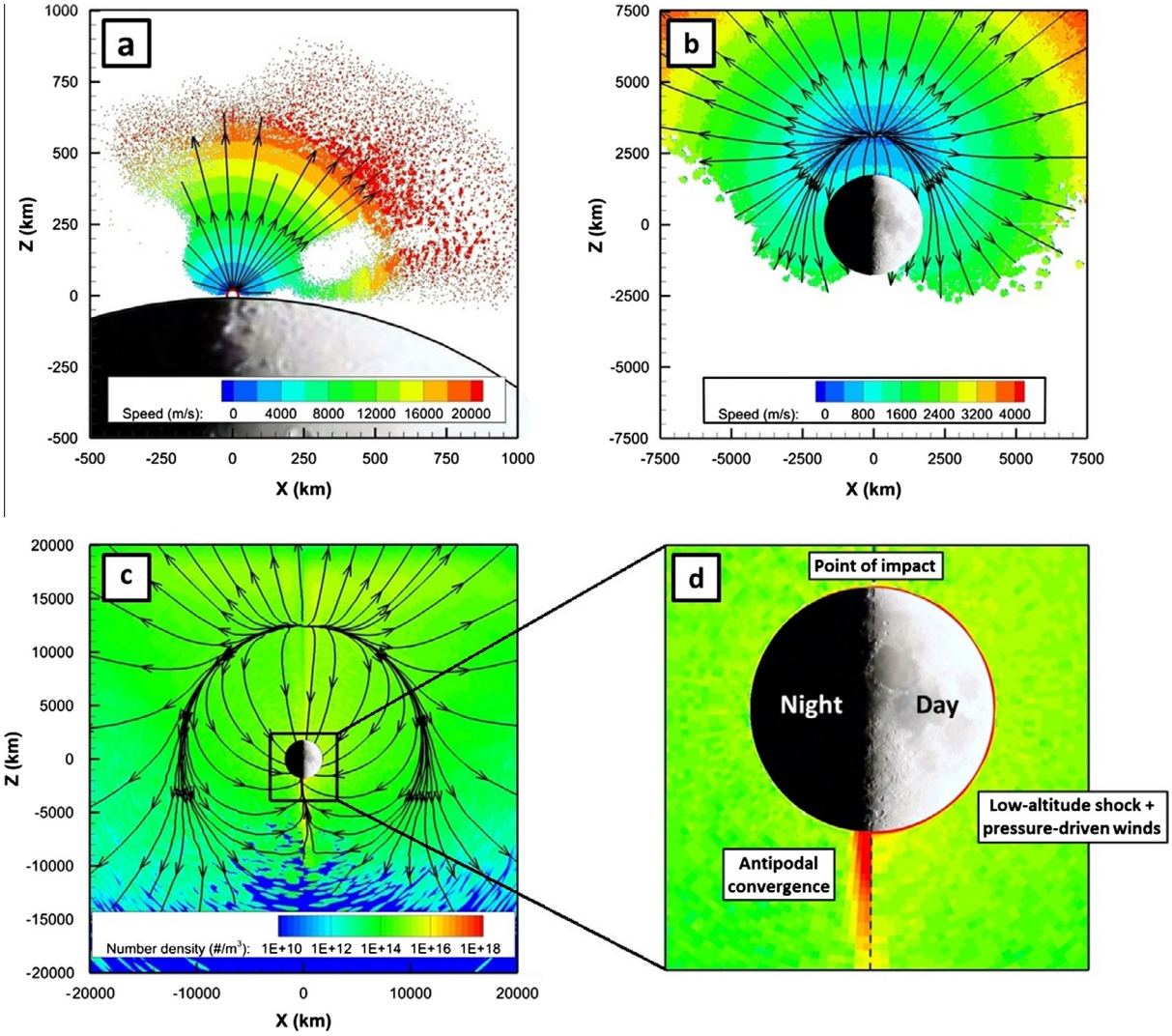

Fig. 2. Cross-sectional views of the transient atmosphere in the plane of impact, at (a) 30 s; (b) 40 min; (c) and (d) 6 h after impact. The image of the lunar surface is included only for perspective: although current simulations do account for diurnal variations in lunar surface temperature, actual topography is not modeled. Colors indicate speed (m/s) in (a) and (b), and number density (molecules/m^3) in (c) and (d). Streamlines, indicating flow direction, are superimposed in (a) to (c). Note differences in color-scale between (a) and (b), and different spatial extents of all four views. (For interpretation of the references to color in this figure legend, the reader is referred to the web version of this article.)

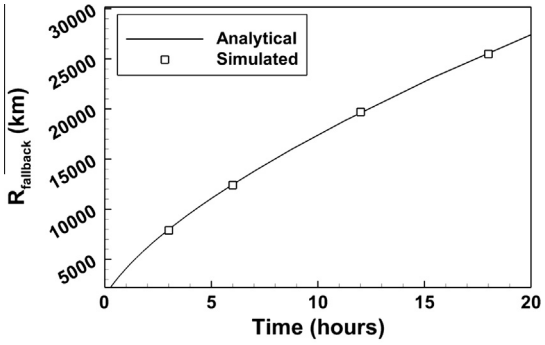

Fig. 3. Comparison of simulated and analytically calculated values of $R_{fallback}$ as a function of time after impact. $R_{fallback}$ is a representative measure of the size of the fallback envelope, defined as the radial distance from the center of the Moon to the fallback envelope as measured through the point of impact.

(Fig. 2(d)). When cold, rarefied, supersonic vapor falling from higher altitudes encounters the pressure of vapor over the day-side, this generates a shock above the day-side hemisphere.

Fig. 4 depicts the structure of the day-side atmosphere in more detail. The streamlines in Fig. 4(a)–(c) show the deceleration and turning of in-falling vapor by a low-altitude shock, giving rise to post-shock winds that sweep over the day-side hemisphere. These winds are driven by global pressure gradients and consequently travel from day-side to night-side and from North to South, for an impact at the North Pole. Over time, more and more vapor is transported from the day-side to the night-side, where it condenses on the cold night-side surface.

Vapor speed decreases gradually, while density increases across the (thick) shock (Fig. 4(a) and (b)). Translational temperature behaves differently (Fig. 4(c)). Cold, in-falling vapor is heated by the shock, but subsequently cools through radiation. Note that due to the relatively low number of simulated molecules in the low density pre-shock region, there is some noise in the DSMC solution, which is most visible in the temperature contours. Also, since we assume thermal accommodation of molecules striking the lunar surface, there is a thin, warm layer adjacent to the surface that cools with altitude, resulting in a cold, intermediate-altitude layer sandwiched between vapor heated by the shock and the lunar day-side.

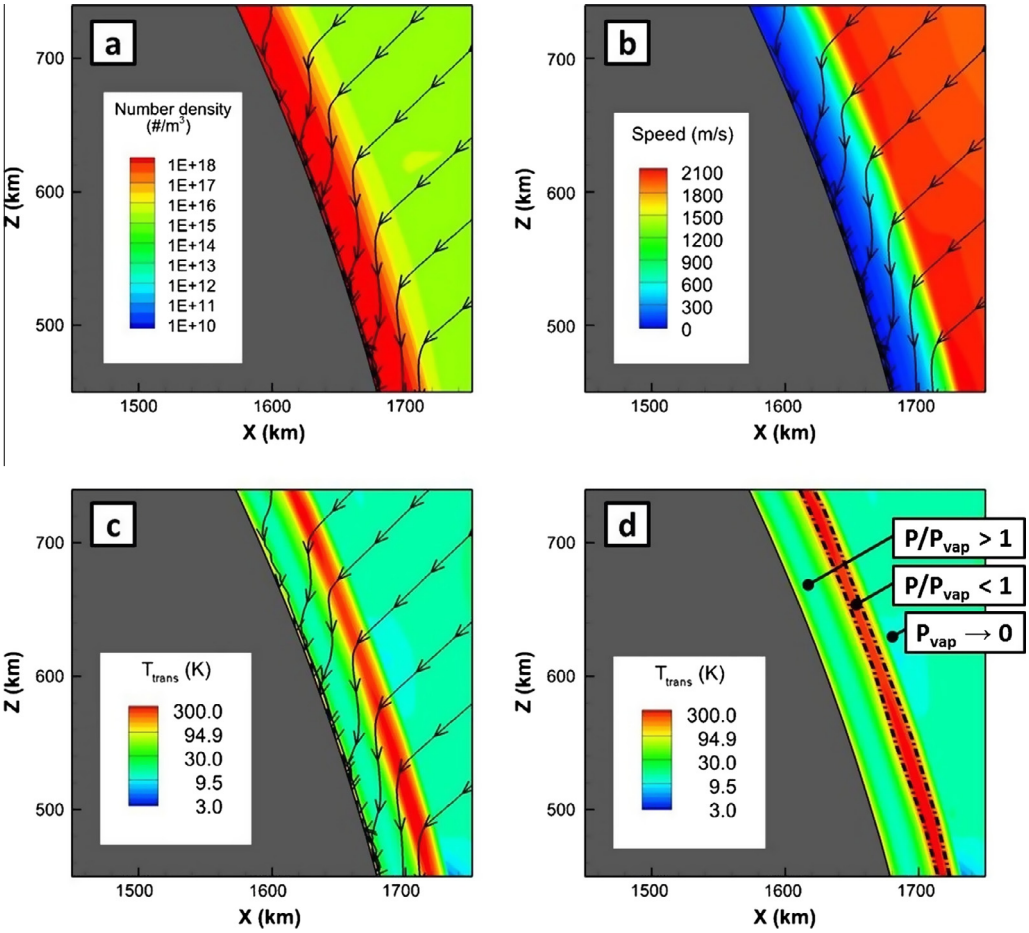

Fig. 4. Cross-sectional views (in the plane of impact) of the low-altitude shock that forms over the lunar day-side, shown at 6 h after impact. The *x*- and *z*-axes indicate distance (km) from the center of the Moon. Contours of (a) number density (molecules/m^3); (b) speed (m/s); and (c), (d) translational temperature (K) show the compression, slowing and heating of water vapor across the shock. Superimposed streamlines in (a) to (c) show the post-shock turning of in-falling vapor. The dotted lines in (d) mark the boundary of the region within which the ratio of kinetic pressure (P) to vapor pressure (P_{vap}) is less than 1. Vapor is supersaturated (i.e. $P/P_{vap} > 1$) above and below this region. However, although $P_{vap} \rightarrow 0$ in the low temperature region above the shock, the lower density of vapor at higher altitudes makes condensation less likely in this region. (For interpretation of the references to color in this figure legend, the reader is referred to the web version of this article.)

The near-surface structure of the transient atmosphere also has implications for the condensation of water vapor. We can compute the saturation water vapor pressure over ice, according to Fleagle and Businger (1980) as follows:

$$P_{vap} = (3.27 \times 10^{12}) \exp(-6119/T_{trans}), \quad (8)$$

where T_{trans} is the translational temperature. This can be compared to the kinetic pressure, given by:

$$P = nk_B T_{trans}, \quad (9)$$

where n is number density. If $P/P_{vap} > 1$, the vapor is super-saturated and could condense in the presence of condensation nuclei (such as lunar or cometary dust). Condensation is not currently modeled, but we note that the vapor is super-saturated above and below the shock-heated layer (Fig. 4(d)). Above the shock-heated layer, although $P_{vap} \rightarrow 0$, the low pre-shock density is unfavorable for condensation. However, condensation could possibly occur in the relatively cold, dense lower layer of the day-side atmosphere if seeded by dust particles, creating a day-side mist or leading to ice crystal or water droplet precipitation. Since vapor pressure is strongly dependent on gas temperature, further investigation of this possibility would require more detailed treatment of radiative heat transfer in the transient atmosphere (without the simplifications discussed in Section 2.2), as well as the consideration of interactions between vapor and dust (of lunar or cometary origin), which are currently not modeled.

Volatile transport in a transient atmosphere, with its characteristic shocks and pressure driven winds, is qualitatively very different from collisionless transport through ballistic hops. Winds should be more effective in transporting water to cold traps and to the shelter of the night-side, since molecules are actively directed by pressure gradients rather than simply wandering over the surface through random walks. The transient atmosphere maintains the general structure discussed above until most of the gravitationally bound vapor has fallen back to the vicinity of the lunar surface, around 48 h after the impact. In the absence of fallback, the surface and antipodal shocks dissipate, but the atmosphere remains collisional, with higher densities over the day-side and around the antipode. Only months after impact does molecular motion become largely collisionless, although the sublimation of night-side frost at sunrise continues to sustain localized collisional transport across the dawn terminator until ultimately, all gravitationally bound water is either photodestroyed or captured (Stewart et al., 2011).

Another factor of interest in an optically thick atmosphere is shielding from photodestruction, which increases the lifetime of molecules, allowing more water to reach the cold traps. Since the lifetime of a water molecule in unattenuated sunlight is ~24 h, the influence of shielding on the structure of the transient atmo-

sphere is not obvious in Fig. 2(c), a snapshot taken just 6 h after impact. However, the structure of the transient atmosphere does have a significant influence on the rate at which water is lost. The photodestruction rate coefficient for water in unattenuated sunlight at 1 AU is 1.2×10^{-5} s^{-1} but it can be seen from Fig. 5 that hours after an impact, there is negligible photodestruction in the dense, post-shock day-side atmosphere, as well as immediately behind the dense antipodal shock. Due to the relatively coarse Cartesian grid used for column density calculations (see Section 2.1), there is some "blockiness" in the rate contours shown in Fig. 5, but selective refinement of the grid in the vicinity of the lunar surface, where all major density jumps take place, allows us to resolve the resulting drops in the intensity of sunlight (and therefore, photodestruction rate) across the day-side and antipodal shocks.

3.3. Night-side frost and cold trap deposits

The distribution and temporal evolution of night-side frost offers some insights into the post-impact volatile transport process. Fig. 6 shows snapshots of the surface concentration (in kg/km^2) of water frost at 6 h and 72 h after impact. Concentrated deposits are seen around the North Pole point of impact and the South Pole antipode. At the times shown, the thickest night-side deposits are O(10^5) kg/km^2. Following the approach of Hodges (2002), a monolayer of water is equivalent to ~0.3 kg/km^2 (or 176 ppm). The lunar night-side therefore has substantially more than a monolayer coating of water. The day-side may also acquire a monolayer coating, since at typical post-shock pressures over the day-side hemisphere, the monolayer formation time is less than a second. However, any subsequent accumulation of water is hindered by low surface residence times (Eq. (1)) at high day-side surface temperatures.

Fig. 6 also shows concentrated bands of frost along the dawn and dusk terminators. The band at the dawn terminator is continuously replenished as frost sublimating at dawn is pushed back across the terminator by day-side winds. In contrast, the band of frost deposited along the original dusk terminator by day-side winds is preserved as the Moon rotates, reflecting the diminishing intensity of fallback from altitude with time.

Fig. 7 tracks the amount of water that is lost (i.e. either photodestroyed or crosses the computational domain boundary at 50,000 km from the lunar surface), and the amount deposited at the North and South Polar cold traps over the course of the 5 Earth days immediately after impact. Although the shock structures discussed in Section 3.2 dissipate 48–72 h after impact as fallback from altitude diminishes, the day-side atmosphere is still collisional 120 h (5 Earth days) later. Interestingly, Fig. 7 indicates that for an impact at the North Pole, antipodal effects lead to deposits at the South Pole that are not only more massive (as anticipated due to the greater cold-trapping area available at the South Pole), but also more concentrated. We find that 5 Earth days after a 60°, 30 km/s impact, the North and South Polar cold traps have accumulated water sufficient to form ice cover O(1 mm) thick over a total area of 5831 km^2 (1257 km^2 at the North Pole and 4574 km^2 at the South pole). It should be noted that, as observed by Stewart et al. (2011), ice deposition continues for several months beyond this, and these numbers will increase as a result. Fig. 7 suggests that a significant part of cold trap deposition may occur before the antipodal shock dissipates, around 48 h after impact. Additionally, Fig. 6 indicates that there are significant non-uniformities in the night-side frost cover even at 72 h after impact, when the antipodal shock has dissipated. This leads to the question of whether the collisional and very non-uniform structure of the transient atmosphere can lead to non-uniform capture of water by cold traps.

Table 1 compares the amount of water captured by the six modeled South Polar cold traps, while Fig. 8 situates these cold traps in the context of transient frost cover. It is observed that Shackleton crater, which happens to coincide with the antipode for the chosen location of impact, maintains the highest concentration of water, consistent with its location where the surface footprint of the antipodal shock is strongest. At 6 h, the cold trap deposit at Shackleton is almost five times as concentrated as the least concentrated deposit, at nearby Cabeus. However, by 72 h, after the antipodal shock has vanished and some slow migration of night side frost

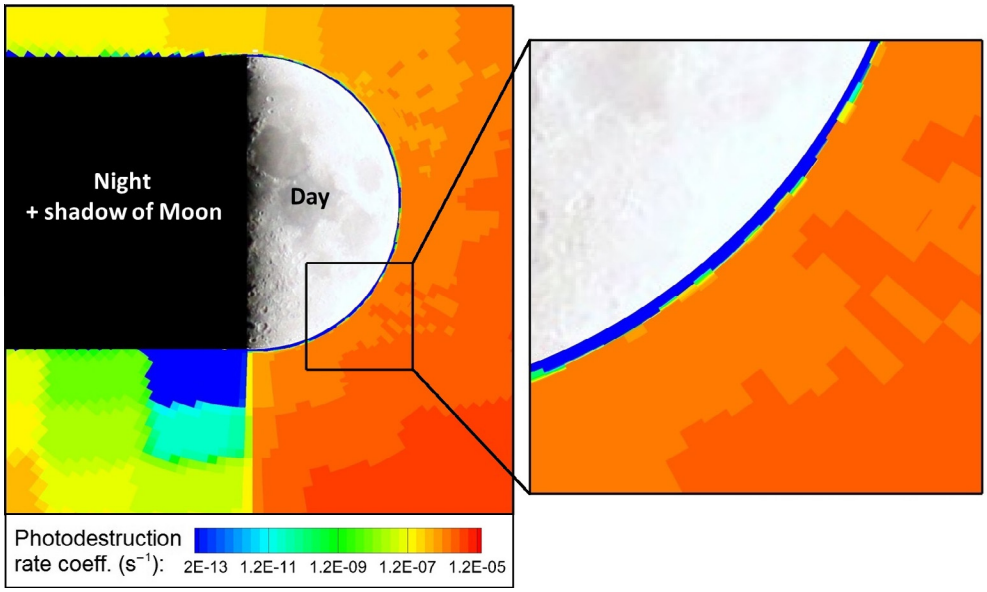

Fig. 5. Photodestruction rate coefficients (s^{-1}) in a cross-section (in the plane of impact) of the water vapor atmosphere at 6 h after impact, when the atmosphere is illuminated by sunlight coming from right to left. Note that the apparent truncation of the shadow cast by the antipodal shock is a computational artifact – because the DSMC grid is spherical, computational cells become larger further away from the N–S axis; the antipodal shock thus blocks only part of the sunlight entering the relatively large cells behind it, so that these cells have a higher total photodestruction rate than the smaller cells closer to the axis that are completely shielded by the antipodal shock. (For interpretation of the references to color in this figure legend, the reader is referred to the web version of this article.)

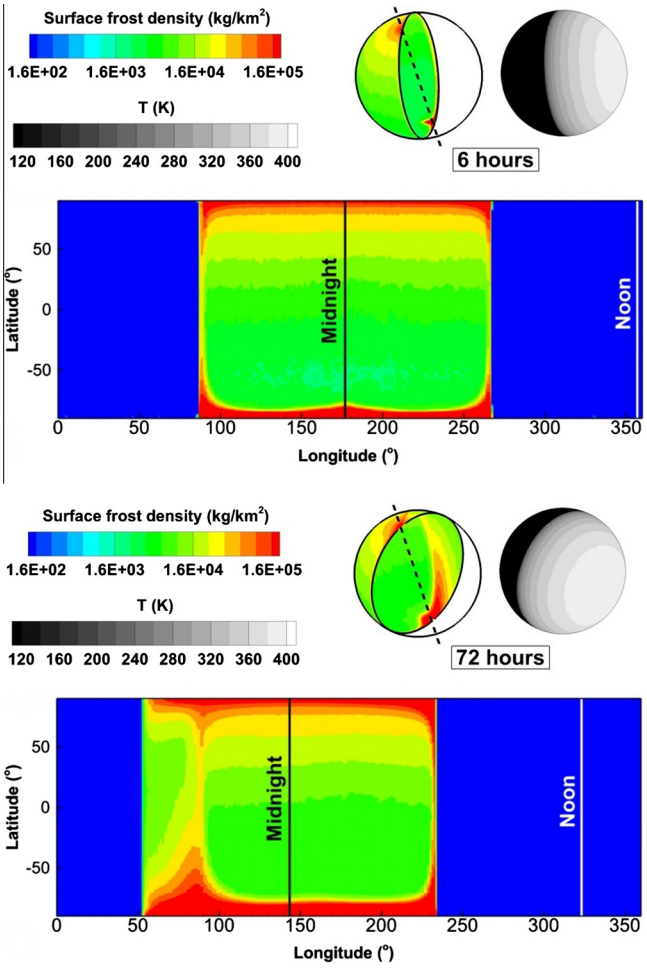

Fig. 6. Cylindrical projections of the lunar surface, showing the change in surface frost patterns between 6 h (top) and 72 h (bottom) after impact. The inset images show cut-away views of the lunar night side (color) and surface temperature (grayscale). Day-side temperatures are too high to allow surface frost cover; the blue regions in the cylindrical projections have virtually no frost. (For interpretation of the references to color in this figure legend, the reader is referred to the web version of this article.)

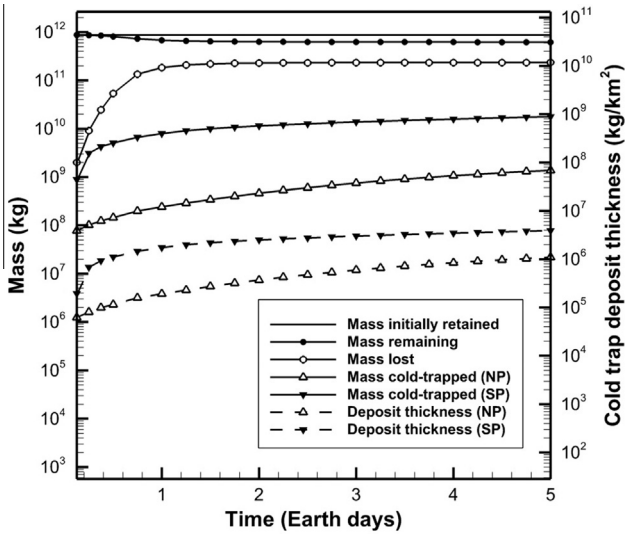

Fig. 7. The amount of water that is lost (i.e. photodestroyed or crosses the computational domain boundary) and cold trapped is tracked over the course of the simulations. Mass and average surface density of cold trap deposits is shown. Also marked is the amount of water initially retained (gravitationally bound) and the amount remaining (aloft or as transient night-side frost).

has taken place, the initial contrast between the different cold traps is somewhat reduced. It is certainly interesting to note that the collisional nature of the impact-generated atmosphere can create non-uniform cold trap deposition patterns. However, longer-term simulations are required to ascertain to what degree initial non-uniformities are preserved as the atmosphere transitions to the collisionless limit and deposition becomes more uniform. It should also be noted that a different impact location could lead to more or less marked differences between cold traps. Currently, the DSMC simulations do not model topography and detailed temperature conditions at individual cold traps, which could increase the heterogeneity of deposition patterns.

3.4. Influence of impact parameters

The simulations discussed here have considered a single set of impact parameters; the modeled impact velocity (30 km/s) and impactor size (radius = 1 km) are representative of Jupiter-family comets, which have a mean encounter velocity of ~20 km/s and estimated radii O(1 km) (Weissman, 2006). In this section, we discuss briefly the influence of varying impact parameters.

It can be seen from Fig. 2(a) that an oblique impact results in downrange focusing of the vapor plume, whereas an impact closer to vertical would yield a more symmetric initial plume (Pierazzo and Melosh, 2000; Stewart et al., 2011). More significantly from the perspective of volatile retention, oblique impacts partition more energy into the projectile (Gisler et al., 2006; Pierazzo and Melosh, 2000), lowering the fraction of vaporized projectile material that is sufficiently slow as to be gravitationally bound. This result is confirmed by comparison of the 60°, 30 km/s impact studied here with the 45°, 30 km/s impact modeled by Stewart et al. (2011). All other impact parameters being the same, ~28% of the comet's mass remains gravitationally bound in the 60 Case, compared to ~3% in the more oblique 45 Case. Ong et al. (2010) find that low velocity impacts play a dominant role in the delivery of lunar water, since more vapor remains gravitationally bound after low velocity impacts. Our preliminary investigations into the influence of impact angle suggest that similarly, although the most probable impact angle is 45° (Pierazzo and Melosh, 2000), less oblique impacts may have made a more significant contribution to the lunar volatile inventory.

Since the transient atmosphere is composed of the fraction of cometary volatiles that remains gravitationally bound, the characteristics that determine this fraction, such as impact energy, obliquity and material properties of the target and impactor, determine the longevity of the transient atmosphere and the degree to which it is collisional. The density of the atmosphere may, in turn, influence the degree of shielding from photodestruction as well as the strength of the shock structures, thereby determining the velocity of post-shock day-side winds and the shape and size of the surface footprint of the antipodal shock i.e. the rate of volatile transport and the nature of deposition patterns.

Another variable parameter is impact location. Since it is difficult to identify conclusively particular lunar craters as having been created by comet impacts, and since any latitudinal variation in impactor flux is likely to be small (Le Feuvre and Wieczorek, 2008), we chose here to simulate an impact at the North Pole in order to minimize certain computational costs. However, as discussed in Section 3.2, a key consequence of the chosen impact location is that the antipodal shock directly intersects the cold night-side; had the impact location been such that the antipode was situated on the day-side, interaction of the antipodal shock with the low-altitude day-side shock could have led to more complex post-

Table 1
Comparison of the amounts of water captured by several different South Polar cold traps at 6 h and 72 h after impact. The lowest and highest concentrations at both times are highlighted. Note that a monolayer of water is equivalent to ~0.3 kg/km^2 or 176 ppm (Hodges, 2002).

Cold trap	Area (km^2)	6 h		72 h	
		Water captured (kg/km^2)	Relative magnitude	Water captured (kg/km^2)	Relative magnitude
Cabeus	897	4.65×10^5	**1.00**	2.80×10^6	1.17
Faustini	697	6.09×10^5	1.31	2.86×10^6	1.20
de Gerlache	314	8.31×10^5	1.79	3.85×10^6	1.61
Haworth	1295	5.75×10^5	1.24	3.01×10^6	1.26
Shackleton	201	2.20×10^6	**4.73**	6.49×10^6	**2.72**
Shoemaker	1170	6.84×10^5	1.47	2.39×10^6	**1.00**

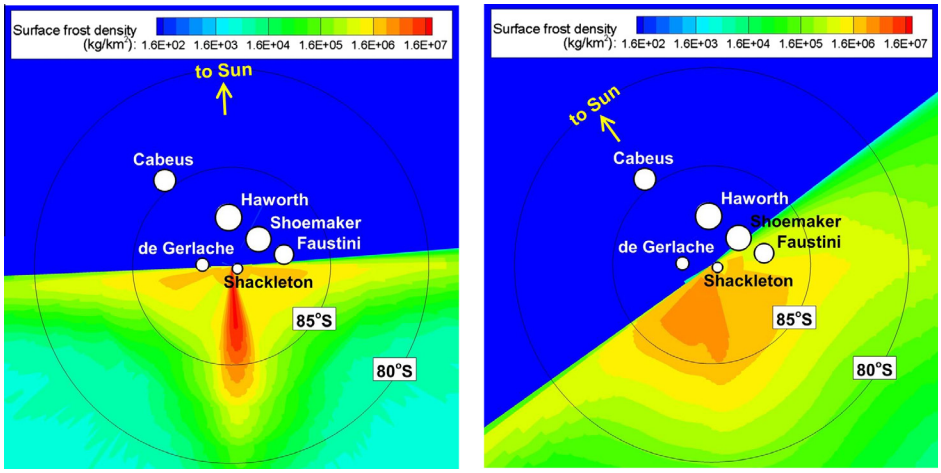

Fig. 8. The simulated South Polar cold traps overlaid on frost density maps, 6 h and 72 h after impact. Cold trap boundaries do not precisely mark the location of actual regions of permanent shadow, but are representative in size. (For interpretation of the references to color in this figure legend, the reader is referred to the web version of this article.)

shock winds and different deposition patterns, a possibility that deserves further investigation.

3.5. Implications for other species

The model adopted in this work currently considers a comet composed only of H_2O ice and neglects photodissociation products, as well as any reactions between them. However, several interesting questions arise from the preceding discussion with respect to how a transient atmosphere would affect and be affected by other volatile compounds. Analytical calculations indicate that over the lifetime of the transient atmosphere, species which are likely to be non-condensable at lunar night-side pressures and temperatures, such as O_2 (Streng, 1971), could accumulate as a result of chemical reactions between photodissociation products (which can only occur when an atmosphere is collisional). This has a direct impact on the cold-trapping process since, as noted by Arnold (1979) and demonstrated by Moore et al. (2009), the presence of less condensable species can slow the rate of condensation of a condensable, such as water. Another noteworthy consequence of multiple species in a collisionally thick atmosphere is that shielding and pressure-driven winds may protect and increase the cold-trapping of species with relatively short photo-lifetimes, which may not be expected to survive long enough to migrate to the shelter of a cold trap if the atmosphere is transparent and migration occurs through diffusive, collisionless hopping.

4. Conclusions

Our objective in this work has been to investigate the processes that govern volatile transport in the aftermath of a volatile-rich impact on an airless body, with a focus on implications for deposition of water at lunar cold traps. This is motivated by Stewart et al.'s (2011) finding that, for representative impact parameters, a significant amount of cold trap capture occurs when impact-generated vapor is in a transitional, collisional state. Therefore, linking current observations of water ice in lunar cold traps to an ancient, transient atmosphere calls for an understanding of how atmospheric gas dynamics influence volatile fallout.

Simulations of the transient atmosphere generated by a comet impact show that within hours, the atmosphere acquires a certain characteristic structure, which it maintains for around 48 h. During this time, volatile transport occurs primarily through pressure-driven winds over the day-side hemisphere, bounded by a low-altitude shock that forms due to the fallback (along near-ballistic trajectories) of cold, rarefied vapor from higher altitude. It is also observed that antipodal convergence of vapor forms a near-cylindrical atmospheric shock that, depending on impact location, can leave a perceptible footprint where it intersects the lunar surface. Although the day-side and antipodal shocks dissipate at around 48 h as the intensity of fallback diminishes, the day-side winds prevail as long as the atmosphere remains collisional. The longevity of a transient atmosphere and the strength of the features identified above depend on specific impact parameters, but its characteristic structure and the nature of transport processes should be similar, whenever an airless body holds a significant quantity of volatiles gravitationally bound after an impact.

When volatiles form a collisionally thick atmosphere, certain physical processes that are otherwise negligible become significant, including shielding from photodestruction, chemical reactions and radiative heat transfer. Our simulations currently account for shielding, but adopt a simplified treatment of radiative

heat transfer that is likely to overestimate radiative cooling at most times. Currently, water is the only species modeled, but several interesting questions that warrant further investigation arise from this work. Does the presence of other species (present in the comet, or formed subsequently through chemical reactions) influence the cold-trapping of water, either by depleting or enhancing the concentration of water through chemical reactions, or by impeding condensation into cold traps? Do interactions between different species and the lunar surface result in preferential condensation of certain compounds, such that the composition of cold trap deposits may not mirror the composition of the impactor?

The fallout from a comet impact is clearly non-uniform, particularly in the vicinity of the antipode, suggesting that the heterogeneities visible in remote sensing observations could partly arise from delivery through an impact. However, late-term, collisionless transport may obscure the sharp non-uniformities seen in short-term fallback patterns and the degree to which this may occur has not yet been studied. Future detailed modeling of topography, surface roughness and illumination conditions in the vicinity of specific cold traps could provide further insight into how these factors influence not just the sequestration of water after deposition, but the deposition process itself.

Acknowledgments

This work was supported by the NASA LASER program under Grant NNX09AM60G. The DSMC simulations would not have been possible without computational resources provided by the Texas Advanced Computing Center. We gratefully acknowledge the contribution of the late Dr. Elisabetta Pierazzo, who carried out a large part of the SOVA simulations at the Planetary Science Institute. We would also like to thank two anonymous reviewers for constructive comments that helped to improve this manuscript.

References

Arnold, J.R., 1979. Ice in the lunar polar regions. J. Geophys. Res. 84, 5659–5668.
Berezhnoi, A.A., Klumov, B.A., 1998. Lunar ice: Can its origin be determined? J. Exp. Theor. Phys. Lett. 68, 163–167.
Berezhnoi, A.A., Klumov, B.A., 2000. Photochemical model of impact-produced lunar atmosphere. Explor. Util. Moon, 175–178.
Bird, G.A., 1994. Molecular Gas Dynamics and the Direct Simulation of Gas Flow. Oxford University Press, New York.
Butler, B.J., 1997. The migration of volatiles on the surfaces of Mercury and the Moon. J. Geophys. Res. 102, 19283–19291.
Cassidy, T.A., Johnson, R.E., 2010. Collisional spreading of Enceladus' neutral cloud. Icarus 209, 696–703.
Colaprete, A. et al., 2010. Detection of water in the LCROSS ejecta plume. Science 330, 463–468.
Combi, M.R., 1996. Time-dependent gas kinetics in tenuous planetary atmospheres: The cometary coma. Icarus 123, 207–226.
Cook, J.C., Stern, S.A., Feldman, P.D., Gladstone, G.R., Retherford, K.D., Tsang, C.C., 2013. New upper limits on numerous atmospheric species in the native lunar atmosphere. Icarus 225, 681–687.
Crider, D.H., Vondrak, R.R., 2000. The solar wind as a possible source of lunar polar hydrogen deposits. J. Geophys. Res. 105, 26773–26782.
Crider, D.H., Vondrak, R.R., 2002. Hydrogen migration to the lunar poles by solar wind bombardment of the Moon. Adv. Space Res. 30, 1869–1874.
Crovisier, J.T., 1984. The water molecule in comets – Fluorescence mechanisms and thermodynamics of the inner coma. Astron. Astrophys. 130, 361–372.
Crovisier, J., 1989. The photodissociation of water in cometary atmospheres. Astron. Astrophys. 213, 459–464.
Feldman, W.C. et al., 2000. Polar hydrogen deposits on the Moon. J. Geophys. Res. 105, 4175–4195.
Fleagle, R.G., Businger, J.A., 1980. An introduction to atmospheric physics. Int. Geophys. Ser. 25, 69–72.
Frenkel, Z., 1924. Theorie der adsorption und verwandter erscheinungen. Z. Phys. 26, 117–138.
Gisler, G.R., Weaver, R.P., Gittings, M.L., 2006. Energy partitions in three-dimensional simulations of the Chicxulub meteor impact. LPSC 37. Abstract 2095.
Gladstone, G.R. et al., 2012. Far-ultraviolet reflectance properties of the Moon's permanently shadowed regions. J. Geophys. Res. 117, E00H04.
Gombosi, T.I., Nagy, A.F., Cravens, T.E., 1986. Dust and neutral gas modeling of the inner atmospheres of comets. Rev. Geophys. 24, 667–700.
Hodges, R.R., 2002. Ice in the lunar polar regions revisited. J. Geophys. Res. 107, 6.1–6.7.
Hood, L.L., Artemieva, N.A., 2008. Antipodal effects of lunar basin-forming impacts: Initial 3D simulations and comparisons with observations. Icarus 193, 485–502.
Huebner, W.F., Keady, J.J., Lyon, S.P., 1992. Solar photo rates for planetary atmospheres and atmospheric pollutants. Astrophys. Space Sci. 195, 1–294.
Langmuir, I., 1916. The evaporation, condensation and reflection of molecules and the mechanism of adsorption. Phys. Rev. 8, 149–176.
Le Feuvre, M., Wieczorek, M.A., 2008. Nonuniform cratering of the terrestrial planets. Icarus 197, 291–306.
Li, S., Milliken, R.E., 2013. Quantitative mapping of lunar surface hydration with Moon Mineralogy Mapper (M^3) data. LPSC 44. Abstract 1337.
Miller, R.S., Lawrence, D.J., Hurley, D.M., 2014. Identification of surface hydrogen enhancements within the Moon's Shackleton crater. Icarus 233, 229–232.
Mitrofanov, I.G. et al., 2010. Hydrogen mapping of the lunar south pole using the LRO neutron detector experiment LEND. Science 330, 483–486.
Moore, C.H., Goldstein, D.B., Varghese, P.L., Trafton, L.M., Stewart, B., 2009. 1-D DSMC simulation of Io's atmospheric collapse and reformation during and after eclipse. Icarus 201, 585–597.
Morgan, T.H., Shemansky, D.E., 1991. Limits to the lunar atmosphere. J. Geophys. Res. 96, 1351–1367.
Nanbu, K., 1986. Theoretical basis of the Direct Simulation Monte Carlo method. In: Rarefied Gas Dynamics: 15th Intl. Symp. Proc., vol. 1, pp. 369–383.
Neish, C.D. et al., 2011. The nature of lunar volatiles as revealed by Mini-RF observations of the LCROSS impact site. J. Geophys. Res. 116, E01005.
Ong, L., Asphaug, E.I., Korycansky, D., Coker, R.F., 2010. Volatile retention from cometary impacts on the Moon. Icarus 207, 578–589.
Paige, D.A. et al., 2010. Diviner lunar radiometer observations of cold traps in the Moon's south polar region. Science 330, 479–482.
Penner, S.S., 1959. Quantitative Molecular Spectroscopy and Gas Emissivities. Addison-Wesley Publishing Company, Inc..
Pierazzo, E., Melosh, H.J., 2000. Hydrocode modeling of oblique impacts: The fate of the projectile. Meteorit. Planet. Sci. 35, 117–130.
Roveda, R., Goldstein, D.B., Varghese, P.L., 2000. Hybrid Euler/Direct Simulation Monte Carlo calculation of unsteady slit flow. J. Spacecraft Rockets 37, 753–760.
Sandford, S.A., Allamandola, L.J., 1993. The condensation and vaporization behavior of ices containing SO_2, H_2S and CO_2: Implications for Io. Icarus 106, 478–488.
Schorghofer, N., Taylor, G.J., 2007. Subsurface migration of H_2O at lunar cold traps. J. Geophys. Res. 112, E02010.
Shuvalov, V.V., 1999. Multi-dimensional hydrodynamic code SOVA for interfacial flows: Application to the thermal layer effect. Shock Waves 9, 381–390.
Siegler, M.A., Bills, B.G., Paige, D.A., 2011. Effects of orbital evolution on lunar ice stability. J. Geophys. Res. 116, E03010.
Spudis, P.D. et al., 2010. Initial results for the north pole of the Moon from Mini-SAR, Chandrayaan-1 mission. Geophys. Res. Lett. 37, L06204.
Stern, S.A., 1999. The lunar atmosphere: History, status, current problems, and context. Rev. Geophys. 37, 453–491.
Stewart, B., Pierazzo, E., Goldstein, D., Varghese, P., Trafton, L., Moore, C. (2009). Parallel 3D hybrid continuum/DSMC method for unsteady expansions into a vacuum. In: Proc. 47th AIAA Aerospace Sciences Meeting, AIAA 2009-266.
Stewart, B.D., Pierazzo, E., Goldstein, D.B., Varghese, P.L., Trafton, L.M., 2011. Simulations of a comet impact on the Moon and associated ice deposition in polar cold traps. Icarus 215, 1–16.
Streng, A.G., 1971. Miscibility and compatibility of some liquid and solidified gases at low temperature. J. Chem. Eng. Data 16, 357–359.
Walker, A.C., Gratiy, S.L., Goldstein, D.B., Moore, C.H., Varghese, P.L., Trafton, L.M., Levin, D.A., Stewart, B., 2010. A comprehensive numerical simulation of Io's sublimation-driven atmosphere. Icarus 207, 409–432.
Watanabe, K., Zelikoff, M., 1953. Absorption coefficients of water vapor in the vacuum ultraviolet. JOSA 43, 753–754.
Watson, K., Murray, B.C., Brown, H., 1961. The behavior of volatiles on the lunar surface. J. Geophys. Res. 66, 3033–3045.
Weissman, P.R., 2006. The cometary impactor flux at the Earth. Proc. Int. Astron. Union, 441–450.
Zhang, J., Goldstein, D.B., Varghese, P.L., Gimelshein, N.E., Gimelshein, S.F., Levin, D.A., 2003. Simulation of gas dynamics and radiation in volcanic plumes on Io. Icarus 163, 182–197.
Zuber, M.T. et al., 2012. Constraints on the volatile distribution within Shackleton crater at the lunar south pole. Nature 486, 378–381.